Reprinted from

THE JOURNAL OF CHEMICAL PHYSICS

Vol. 104, No. 22, 8 June 1996

Molecular radiative transport. II. Monte-Carlo simulation

E. J. Nunes Pereira, M. N. Berberan-Santos, and J. M. G. Martinho
Centro de Química-Física Molecular, Instituto Superior Técnico, 1096 Lisboa Codex, Portugal

pp. 8950–8965

AMERICAN INSTITUTE OF PHYSICS

Molecular radiative transport. II. Monte-Carlo simulation

E. J. Nunes Pereira, M. N. Berberan-Santos, and J. M. G. Martinho
Centro de Química-Física Molecular, Instituto Superior Técnico, 1096 Lisboa Codex, Portugal

(Received 12 December 1995; accepted 1 March 1996)

The theory of radiative transport allows in principle the accurate calculation of the fluorescence intensity and anisotropy decays, and of the fluorescence spectrum and macroscopic quantum yield, under given conditions. However, most of the coefficients of the theoretical expressions are in general not amenable to analytic form, and even their numeric computation is quite difficult. Given the probabilistic nature of the underlying processes of absorption and emission, a Monte-Carlo (MC) simulation built upon the basic theoretical equations is particularly well suited for the task. In this work, we discuss and carry out detailed simulations for a realistic system (rhodamine 101 in ethanol) in a finite three-dimensional volume that reproduces a common fluorescence cell. The two usual geometries of detection are considered: front face and right angle. The MC simulation method developed allows, for the first time, the accurate calculation of the effect of radiative transport on fluorescence intensity and anisotropy decays, time-resolved and steady-state spectra, as well as on the values of the macroscopic quantum yield and steady-state anisotropy. Because the spatial distribution of each generation of excited molecules can also be obtained with this method, a direct and clear picture of the spatial evolution of the excitation is also obtained. © *1996 American Institute of Physics.* [S0021-9606(96)51521-7]

I. INTRODUCTION

In assemblies of like atoms or molecules the photons emitted by electronically excited species may be reabsorbed and re-emitted several times before they can leave the sample. This phenomenon is known as radiation imprisonment, radiative migration, or radiative transport. Its importance depends on many factors: extent of spectral overlap between absorption and emission, fluorescence quantum yield, concentration, cell size and shape, detection geometry, etc. When present, this process affects the fluorescence decays and spectra, as well as the fluorescence anisotropy.

In Paper I of this work,[1] a complete stochastic theory of radiative transport was presented. With this theory, that contains no adjustable parameters, it is possible to accurately predict the effect of radiative migration on the fluorescence intensity and anisotropy decays, and on the fluorescence spectrum, under given conditions. However, most of the coefficients of the laws derived are in general not amenable to analytic form, and even their numerical computation is quite difficult. Given the probabilistic nature of the underlying processes of absorption and emission, a Monte-Carlo (MC) simulation built upon the basic theoretical equations derived before[1] is particularly well suited for the task. In this work, we discuss and carry out detailed simulations for a realistic system (rhodamine 101 in ethanol) in a finite three-dimensional volume that reproduces a common fluorescence cell.

The MC simulation method developed allows, for the first time, the accurate calculation of the effect of radiative transport on fluorescence intensity and anisotropy decays, time-resolved and steady-state spectra, as well as on the values of the macroscopic quantum yield and steady-state anisotropy. Because the spatial distribution of each generation of excited molecules can also be obtained with this method, a direct and clear picture of the spatial evolution of the excitation under given conditions is also obtained.

In Sec. II, we start by stating the scope and assumptions of the simulations (Sec. II A), and then present the basic equations of radiative transport for the ensemble decay law and macroscopic quantum yield (Sec. II B), angular dependence (Sec. II C) and time-resolved and steady-state anisotropies (Sec. II D). We then describe the Monte-Carlo simulation (Sec. III). In Secs. IV and V, the results of extensive simulations for a dye (rhodamine 101 in ethanol) in front-face (Sec. IV) and right-angle (Sec. V) geometries in finite three-dimensional and also in semi-infinite volumes are discussed. The fluorescence spectrum and quantum yield, the steady-state and time-resolved fluorescence intensity and anisotropy are examined as a function of concentration, excitation, and emission wavelengths and size of the cell.

II. THEORY

A. Scope and assumptions

Consider a given volume of convex but otherwise arbitrary shape containing a macroscopically uniform distribution of identical molecules. We give here equations for the time evolution of the intensity and polarization of the fluorescence emitted by the molecular ensemble, in response to excitation by an external beam of linearly polarized and essentially monochromatic light.[1] The duration of the excitation flash may range from a few femtoseconds to several minutes. In the first case the time-dependent fluorescence emitted is called the δ response or decay law, while in the second case (continuous irradiation) it is called the steady-state (photostationary-state) intensity. If the excitation beam intensity is low, that is, nonsaturating, the δ response can be used to obtain the response to any kind of time-dependence for the excitation, including the photostationary state. We

 0021-9606/96/104(22)/8950/16/$10.00

assume this to be valid, and use the results for the δ response, from which the photostationary state can then be derived. The model also assumes that absorption and fluorescence are homogeneously broadened, i.e., that a single type of molecule is present.

The fluorescence emitted by the molecular ensemble is in general anisotropic, regarding both intensity and time dependence. Besides being dependent on the directions of excitation and detection, the δ response is a function of molecular spectroscopic properties: fluorescence lifetime and fluorescence quantum yield, emission and absorption spectra. In this way, it depends on the excitation and emission wavelengths, on the molecular concentration and on the sample size and shape. The optics at the boundaries (refraction, internal reflection) also play a role, as discussed in Sec. III.

B. Ensemble decay law and macroscopic quantum yield

The (un-normalized) ensemble decay law (for all directions, that is, 4π) can be written as (for nonspherical samples, the excitation direction should also be specified; this is not done explicitly in order not to overload the notation)

$$\rho(\lambda_{exc},\lambda_{em},t)=\sum_{n=1}^{\infty}\rho_n(\lambda_{exc},\lambda_{em},t), \tag{1}$$

where $\rho(\lambda_{exc},\lambda_{em},t)$ is the probability that a photon of wavelength λ_{em} will leave the sample between t and $t+dt$, given that a photon of wavelength λ_{exc} was absorbed at time $t=0$, and $\rho_n(\lambda_{exc},\lambda_{em},t)$ is the probability that a photon of wavelength λ_{em} will leave the sample between t and $t+dt$ after exactly n absorption–emission events, given that a photon of wavelength λ_{exc} was absorbed at time $t=0$. This last probability is

$$\rho_n(\lambda_{exc},\lambda_{em},t)=p_n(\lambda_{exc},\lambda_{em})\rho_n(t), \tag{2}$$

where $p_n(\lambda_{exc},\lambda_{em})$, mean escape probability, is the probability that a photon leaves the sample after exactly n absorption–emission events and has wavelength λ_{em}, given that a photon of wavelength λ_{exc} was absorbed; and $\rho_n(t)$ is the probability that a nth generation molecule will emit a photon between t and $t+dt$, given that it will emit one. This probability (normalized density function) is given by[1]

$$\rho_n(t)=\frac{1}{\tau_0}\frac{(t/\tau_0)^{n-1}}{(n-1)!}\exp\left(-\frac{t}{\tau_0}\right), \tag{3}$$

where τ_0 is the molecular lifetime.

The decay law is therefore written as

$$\rho(\lambda_{exc},\lambda_{em},t)=\sum_{n=1}^{+\infty}p_n(\lambda_{exc},\lambda_{em})\frac{1}{\tau_0(n-1)!}\times\left(\frac{t}{\tau_0}\right)^{n-1}\exp\left(-\frac{t}{\tau_0}\right), \tag{4}$$

and we can define a mean fluorescence intensity lifetime corresponding to this decay law as

$$\tau(\lambda_{exc},\lambda_{em})=\frac{\int_0^{+\infty}t\rho(\lambda_{exc},\lambda_{em},t)dt}{\int_0^{+\infty}\rho(\lambda_{exc},\lambda_{em},t)dt}=\left\{\frac{\sum_{n=1}^{+\infty}np_n(\lambda_{exc},\lambda_{em})}{\sum_{n=1}^{+\infty}p_n(\lambda_{exc},\lambda_{em})}\right\}\tau_0, \tag{5}$$

the term between brackets being, in some sense, a mean number of reabsorption/re-emission events corresponding to the emission detected at λ_{em}.

On the other hand, $\rho_n(\lambda_{exc},\lambda_{em})$ can be written as[1]

$$p_n(\lambda_{exc},\lambda_{em})=\Phi_0^n\int f(\mathbf{r}_1|\lambda_{exc})d\mathbf{r}_1\times\int F_0(\lambda_1)\int f(\mathbf{r}_2|\mathbf{r}_1,\lambda_1)d\mathbf{r}_2d\lambda_1\cdots\times\int F_0(\lambda_{n-1})\int f(\mathbf{r}_n|\mathbf{r}_{n-1},\lambda_{n-1})\times d\mathbf{r}_n d\lambda_{n-1}\times F_0(\lambda_{em})\left[1-\int f(\mathbf{r}|\mathbf{r}_n,\lambda_{em})d\mathbf{r}\right], \tag{6}$$

where Φ_0 is the molecular quantum yield, $f(\mathbf{r}_i|\mathbf{r}_{i-1},\lambda_{i-1})$ is the probability (density function) that a photon of wavelength λ_{i-1} and emitted at $\mathbf{r}_{i-1}$ will be reabsorbed at $\mathbf{r}_i$, and is given by[1]

$$f(\mathbf{r}_i|\mathbf{r}_{i-1},\lambda_{i-1})=\frac{1}{4\pi|\mathbf{r}_i-\mathbf{r}_{i-1}|^2}\varepsilon(\lambda_{i-1})\times C\ln 10\,10^{-\varepsilon(\lambda_{i-1})C|\mathbf{r}_i-\mathbf{r}_{i-1}|} \tag{7}$$

and $f(\mathbf{r}_1|\lambda_{exc})$, which is the probability of absorption at $\mathbf{r}_i$ of the excitation photon, is given by

$$f(\mathbf{r}_1|\lambda_{exc})=\frac{\varepsilon(\lambda_{exc})C\ln 10\,10^{-\varepsilon(\lambda_{exc})Cr_1}}{\int_0^{r_{max}}\varepsilon(\lambda_{exc})C\ln 10\,10^{-\varepsilon(\lambda_{exc})Cr_1}dr_1}, \tag{8}$$

where $\epsilon(\lambda)$ is the molar absorption coefficient, C is the molar concentration and r_{max} is the maximum pathlength along

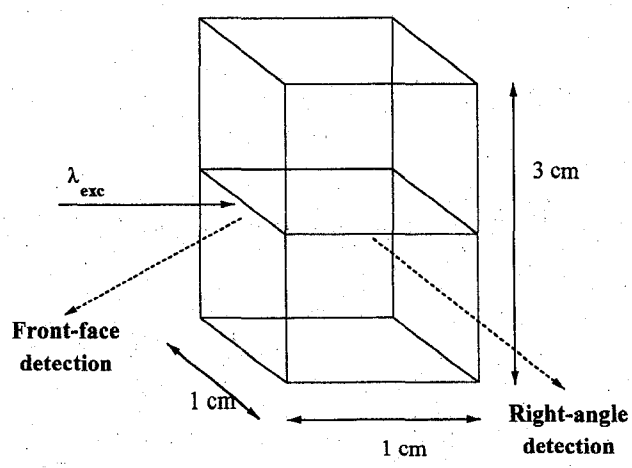

FIG. 1. Tridimensional cell used in MC simulation.

the excitation direction. The integration in wavelength runs in principle from zero to infinity, but the effective maximum wavelength is the absorption cutoff λ_c, beyond which the probability of absorption is zero. Equation (7) is also based on the assumption of isotropic emission, which implies significant molecular rotation during the intrinsic molecular lifetime.

The macroscopic fluorescence quantum yield is given by

$$\Phi(\lambda_{exc}) = \int_0^\infty \int_0^\infty \rho(\lambda_{exc},\lambda_{em},t)dt\ d\lambda_{em} = \sum_{n=1}^\infty \int_0^\infty p_n(\lambda_{exc},\lambda_{em})d\lambda_{em}. \quad (9)$$

C. Angular dependence

The fluorescence is usually collected at a certain angle from the excitation beam, the front-face and right-angle geometries being the two most common situations (Fig. 1). The experimental decay collected at a certain angle (within a narrow cone) may differ significantly from the orientationally integrated (or ensemble) decay. Indeed, the probability of emission for a given direction Ω, ρ^Ω, is given by

$$\rho^\Omega(\lambda_{exc},\lambda_{em},t) = \sum_{n=1}^\infty p_n^\Omega(\lambda_{exc},\lambda_{em})\rho_n(t), \quad (10)$$

where

$$p_n^\Omega(\lambda_{exc},\lambda_{em}) = \int f(\mathbf{r}_1|\lambda_{exc})d\mathbf{r}_1\Phi_0 \int \int F_0(\lambda_1)f(\mathbf{r}_2|\mathbf{r}_1,\lambda_1)d\mathbf{r}_2\ d\lambda_1 \cdots \times \cdots \Phi_0 \int \int F_0(\lambda_{n-1})f(\mathbf{r}_n|\mathbf{r}_{n-1},\lambda_{n-1})d\mathbf{r}_n\ d\lambda_{n-1}\frac{1}{4\pi}\Phi_0 F_0(\lambda_{em})\left[1-\int_0^{r_{max}(\Omega)} f(r|\mathbf{r}_n,\lambda_{em})dr\right] \quad (11)$$

and

$$f(r|\mathbf{r}_n,\lambda_{em}) = \varepsilon(\lambda_{em})C\ \ln 10\ 10^{-\varepsilon(\lambda_{em})Cr} \quad (12)$$

so that

$$\rho(\lambda_{exc},\lambda_{em},t) = \int \rho^\Omega(\lambda_{exc},\lambda_{em},t)d\Omega. \quad (13)$$

D. Time-resolved and steady-state anisotropies

For the purpose of computing the effect of radiative transport on fluorescence anisotropy, we consider only measurements made in directions contained in the horizontal plane (denoted $\perp$, and including the front-face and right-angle geometries), for which the anisotropy of fluorescence takes the highest value. We further suppose that molecular rotational motion is negligible during the lifetime and that the exciting photons carry vertical polarization.

The time dependent anisotropy is given by

$$r(\lambda_{exc},\lambda_{em},t) = r_1(\lambda_{exc})\frac{\sum_{n=1}^\infty p_n^\perp(\lambda_{exc},\lambda_{em})\rho_n(t)\beta^{n-1}}{\sum_{n=1}^\infty p_n^\perp(\lambda_{exc},\lambda_{em})\rho_n(t)}, \quad (14)$$

where $r_1(\lambda_{exc})$ is the anisotropy of fluorescence of directly excited molecules (the so-called fundamental anisotropy), and β is the depolarization factor (β=0.28).[1]

The steady-state anisotropy is

$$\bar{r}(\lambda_{exc},\lambda_{em}) = r_1(\lambda_{exc})\frac{\sum_{n=1}^\infty p_n^\perp(\lambda_{exc},\lambda_{em})\beta^{n-1}}{\sum_{n=1}^\infty p_n^\perp(\lambda_{exc},\lambda_{em})}. \quad (15)$$

It should be remarked that, for exact results, the $p_n^\perp(\lambda_{exc},\lambda_{em})$ of Eqs. (14) and (15) must be computed with a reabsorption probability whose orientational dependence is that of a radiating electric dipole, and not that of an isotropic emitter, Eq. (7), because it is now assumed that molecular rotation is essentially frozen within the intrinsic lifetime. However, the results are expected not to greatly differ. It should also be mentioned that the fluorescence anisotropies computed from Eqs. (14) and (15) completely neglect the contribution from nonradiative transport, which may dominate for the cases where the average distance between molecules is smaller or of the order of the Förster radius for self-transfer.

III. THE SIMULATION PROCEDURE

A. General considerations

Because of the factorization of space and time dependencies in $\rho_n(\lambda_{exc},\lambda_{em},t)$ [Eq. (2)] and since the exact time dependence is known [Eq.(3)], the simulation procedure can be restricted to the spatial aspects of radiative transport, which means an important gain in simulation efficiency. The goal is therefore the evaluation of the mean escape probabilities [whether or not orientationally integrated—see Eqs. (6) and (11)], and from these, the decay law [Eq. (4)]. Similarly, the macroscopic quantum yield [Eq. (9)] and the time dependent and steady-state anisotropies [Eqs. (14) and (15)] can be computed from the knowledge of the $p_n^\Omega(\lambda_{exc},\lambda_{em})$ for appropriate values of Ω.

The Monte-Carlo (MC) method[2,3] is used to directly reproduce the random flight of photons within the defined vol-

ume. Radiative transport is intrinsically stochastic: The photon emission wavelength, the emission direction, and the photon pathlength are all random quantities obeying known distribution functions. Random numbers were obtained as described before.[4] These random numbers were used in each elementary step to decide (a) whether the excited molecule decayed radiatively or nonradiatively, (b) the photon emission direction, (c) the fluorescence wavelength, and (d) the photon pathlength.

The MC simulations were carried out for two different geometries. A fully 3D simulation of the energy migration in a finite tridimensional volume (fluorescence cell) and a unidimensional equivalent of a semi-infinite tridimensional space. The bulk of the work was carried out for the first case, the chosen volume being a conventional $1\times1\times3$ (z coordinate) cm cell that for computational purposes was sliced in 48.000 volume elements of $0.25\times0.25\times1$ (z) mm.

All favorable simulation runs were terminated only after the 25th generation was attained, thus assuring that the truncation of the number of generations did not influence the results: For the worst case in front face, the maximum contribution of the last generation to the overall decay was only 0.008%.

For each set of parameters, simulation of individual photon trajectories was repeated until the termination conditions—a predefined fractional accuracy of 0.005% in overall decays and in real quantum yield—were satisfied. The test on termination conditions was implemented as follows. The data estimated by the MC simulation are given as a statistical best estimate of 20 data points which correspond to individual estimates of escape probabilities for different numbers of counts in the first generation (seen by the detector). At intervals of 2.5 million of counts for the first generation (starting only at 100 million counts to ensure at least a moderate statistical convergence) the program computes one data point for all the parameters and for all the trajectories simulated thus far. Every 5 new data points, that is, every $5\times2.5=12.5$ million new counts, it computes one approximation of the simulation parameters making use of 20 data points (thus spanning $20\times2.5=50$ million counts) as if they were 20 different and independent measures of some physical quantity (which is not strictly the case; the 20 data points are not statistically unrelated as can easily be seen from the fact that each one differs from the previous one just by considering 2.5 million new additional trajectories). Nevertheless, several tests were made, all of them showing that it is always considered a sufficient high number of trajectories to ensure that the parameters converge to a statistically significant value.

The termination condition is the attainment of a predetermined minimum fractional accuracy of 0.005% in steady-state emission and in predicted real quantum yield. The program computes sample means, variances, and covariances and uses these values to estimate the predicted fractional accuracies by standard error analysis. These are then tested against termination conditions.

All the simulations were made on a DEC ALPHA AXP 2300 under OPEN VMS / FORTRAN compiler and the CPU times ranged from 7 h to about one week depending on the relative importance of energy migration.

B. Spatial distribution functions of the excited generations

The spatial distribution functions of excited molecules, grouped in generations (directly excited molecules belonging to the first generation, molecules excited by absorption of photons emitted by first generation molecules belonging to the second generation, and so on) were obtained directly from the number of molecules of each generation in each volume element. The plots shown in Figs. 4 and 14 refer to the horizontal layer at half-height, which contains the external excitation beam (Fig. 1), and whose thickness is 1 mm, as mentioned.

C. Escape probabilities

Knowledge of the mean escape probabilities is essential for the computation of fluorescence intensity decays, macroscopic quantum yield, and steady-state and time-resolved anisotropies, whether angular dependent or orientation integrated.

The computation of the escape probabilities requires an integration over all possible photon trajectories, cf. Eqs. (6) and (11). These trajectories are random flights with a wide distribution of jump lengths x, $f(x)$,

$$f(x)=\int_0^\infty F_0(\lambda)\varepsilon(\lambda)\ln 10\, C\, 10^{-\varepsilon(\lambda)Cx}\, d\lambda. \tag{16}$$

The average pathlength computed from Eq. (16) is usually infinite. This result implies that a diffusion equation (Brownian motion) does not hold for the problem, a point already addressed by Holstein.[5] The infinite value for the average pathlength could be naively interpreted as resulting from the fact that a significant part of the emission falls beyond the cut-off wavelength and is not reabsorbed. However, the result may still persist without a cut-off wavelength, as is the case with two Gaussian functions, one for the absorption spectrum and other for the emission spectrum. Indeed, the photon random motion is in these conditions a hyperdiffusive but nonfractal (non-Lévy stable[6]) flight. For the specific geometry under consideration (fluorescence cell), the space is finite, because the walls of the cell act as absorbing barriers. Therefore, the effective pathlength is always finite.

For the simulation of the trajectories Eq. (7) was recast in spherical coordinates,

$$f(\mathbf{r}_i|\mathbf{r}_{i-1},\lambda_{i-1})=\frac{\sin\theta}{4\pi}\varepsilon(\lambda_{i-1})C\ln 10\, 10^{-\varepsilon(\lambda_{i-1})Cr} \tag{17}$$

$[\sin\theta/(4\pi)]$ being the emission angular distribution (assumed isotropic) the rest of the equation being the absorption probability only dependent on the distance $r=|\mathbf{r}_i-\mathbf{r}_{i-1}|$ (isotropic absorption). Three independent draws of the random number generator were then used to decide the photon emission direction (spherical angles θ and φ) and the photon

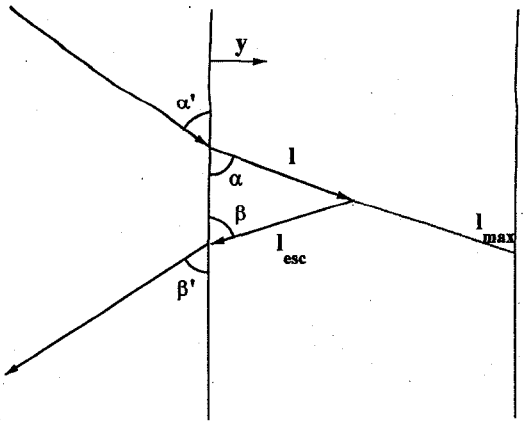

FIG. 2. Top view of the front-face geometry, including refraction at cell boundary.

pathlength relative to emission point (r), the cartesian coordinates being then straightforwardly computed.

For front-face geometry in high concentrated media one can consider that the variable controlling the escape probability towards the detector is solely the distance between the emission point and the cell wall exposed to external excitation (and facing the detection system). This corresponds to the simulation of small penetration of external excitation and to a very small mean photon pathlength. In this limit case, the full 3D simulation reduces to a unidimensional equivalent, by simply integrating the 3D transition probability, Eq. (7), over different layers with the same distance to the cell wall [Appendix— Eq. (A1)]. In doing so, computational efficiency is gained because the discretized cell becomes a unidimensional vector, although the corresponding pathlength distribution is more complex (Appendix). In this way, two different transition probability functions were used for the MC simulation: either Eq. (17) for the 3D simulation, or its unidimensional equivalent, Eq. (A1), for the 1D simulation.

Equation (8) was always used for the computation of the absorption coordinates of external excitation. This equation is simply the usual Beer–Lambert law along a single linear pathlength, the only special care being the need to consider that the pathlength defined by external excitation is only normal to the impinging excitation wall for the right-angle geometry. For the unidimensional simulation it was then necessary to correct this pathlength to the simulation coordinate by multiplying the linear path by a geometrical parameter accounting for the excitation geometry. This factor follows from Snell's refraction law and the relevant equivalent of Eq. (8) for the unidimensional simulation is

$$f(y|\lambda_{exc}) = \frac{\varepsilon(\lambda_{exc})C \ln 10\, 10^{-\varepsilon(\lambda_{exc})C\left\{1-\left(\frac{\cos\alpha'}{n}\right)^2\right\}^{1/2} l}}{\int_0^{l_{max}} \varepsilon(\lambda_{exc})C \ln 10\, 10^{-\varepsilon(\lambda_{exc})Cl}\, dl} \tag{18}$$

n being the refractive index (Fig. 2). Note that the relevant coordinate for the unidimensional simulation is the distance to the cell wall probed by the detector, i.e., coordinate y.

For the computation of the macroscopic ensemble fluorescence quantum yield [Eq. (9)] it is necessary to know the angular and emission wavelength integrated escape probabilities. These are given by the ratio of the number of photons emitted by nth generation molecules that are not reabsorbed to the total number of excitation trajectories simulated.

In front-face geometry, the detection direction is defined by the angle β' shown in Fig. 2. The angle that the radiation should have inside the cell in order to be detected, β, is then given by Snell's law. From β' and from the emission coordinates, the linear pathlength l_{esc} along which radiation can be reabsorbed is computed. Finally, the escape probability for this pathlength is given by

$$p_{esc}(\lambda_{em}) = 10^{-\varepsilon(\lambda_{em})Cl_{esc}}. \tag{19}$$

For the full 3D simulation an additional constraint was imposed: Detection was effective only for molecules located inside a cylinder defined by the angle β and by a circle of 5 mm diameter on the frontal face of the cell. Only the photons emitted inside the cylinder that hit the circle at the wall were taken into account, with an escape probability given by Eq. (19).

For the 1D simulation, two different cases were considered. First, an equivalent of the 3D one [Eq. (18)], that is, a single direction for detection. A second case was considered corresponding to the detection of all escaping photons, that is, through a π solid angle collection, Eq. (A3). In these two cases, the relevant distance is always the distance to the cell wall probed by the detection.

As regards the right-angle detection, only a 3D simulation was considered. The 5 mm effective circle for detection was used in the way already described for front-face detection.

During the simulation of the photon trajectories, the program keeps track of the global escape probabilities for each generation and detection wavelength, i.e., whenever a photon emitted by a nth generation molecule contributes to the observed decay, the program increments a counter by the corresponding value given by Eq. (19). At the end of the simulation, the mean escape probabilities in the direction defined by Ω and at wavelength λ_{em}—$p_n^{\Omega}(\lambda_{exc},\lambda_{em})$ in Eq. (11)—are estimated as the ratio of the corresponding counter to the total number of excitation photons absorbed.

D. System studied

The MC simulation of the radiative transport of electronic excitation energy was carried out for the system rhodamine 101 in acidified ethanol (Fig. 3). This system is particularly suitable due to the combination of several factors favoring radiative transport—high absorption–emission spectral overlap (ca. 87%), high fluorescence quantum yield (89%), and high molar absorption coefficients in the overlap region. These factors also favor nonradiative transport; indeed, under the same experimental conditions we calculate a Förster critical radius of 58 Å, and estimate that for the most concentrated solution (10^{-3} M) ca. 50% of the excited mol-

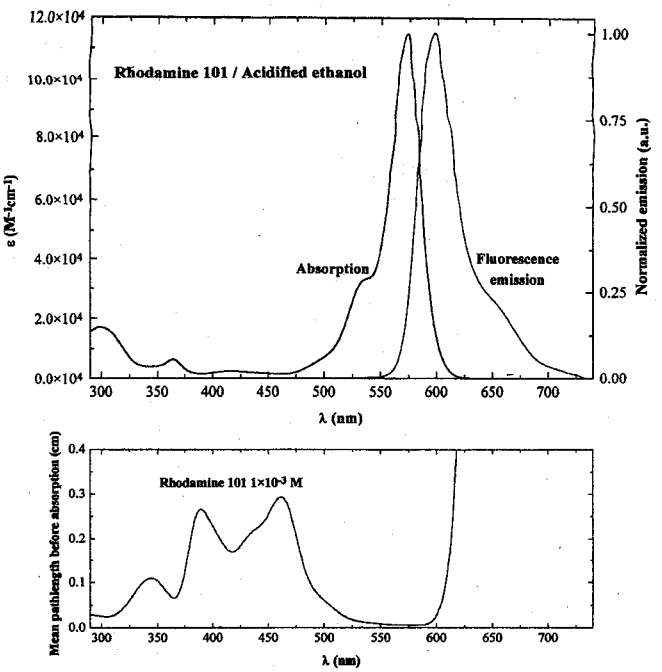

FIG. 3. Absorption and fluorescence spectra of rhodamine 101 in acidified ethanol at room temperature. Shown is also the mean pathlength of photons for a solution 10^{-3} M in rhodamine 101.

ecules undergo nonradiative energy transfer. Fluorescence intrinsic emission spectra and quantum yield were experimentally determined in a dilute (5×10^{-7} M) solution of the dye. The emission yield was estimated by a relative method. The molecular lifetime, 4.34 ns, was also experimentally measured for the dilute solution. Four different excitation wavelengths are used throughout the work: 294 nm ($\epsilon = 1.6\times10^4$ M^{-1} cm^{-1}), 300 nm ($\epsilon = 1.7\times10^4$ M^{-1} cm^{-1}), 520 nm ($\epsilon = 1.9\times10^4$ M^{-1} cm^{-1}), and 570 nm($\epsilon = 1.1\times10^5$ M^{-1} cm^{-1}). The first three correspond to a higher penetration depth (roughly equal) of the incoming external excitation than the fourth (see Fig. 3).

Extensive results are presented for both front-face and right-angle geometries. Results for the front-face geometry are first discussed in Sec. IV, the right-angle geometry results being presented in Sec. V.

IV. FRONT-FACE GEOMETRY

A. Spatial distribution functions

Figure 4 shows contour plots of the spatial distribution functions of selected generations in the horizontal plane containing the excitation beam.

The progressive spread of the excitation as time evolves is apparent. As mentioned above, the process is nondiffusive. Moreover, since the closer to the cell wall the higher the escape probability, there is also a progressively deeper penetration of the excitation into the cell. In this way, the probability of excitation for late generations peaks inside the cell, while that of the first generations has its maximum at the cell boundary. The flamelike shape of some of the plots is striking, and is also due to the high escape probabilities for photons emitted near the wall.

The first part of the figure (first two rows) show results for high penetration of external excitation while the second part corresponds to a much smaller penetration ($\epsilon_{570\ nm}$ is roughly 10 times $\epsilon_{294\ nm}$). One can see that even for a concentration 10^{-4} M and an important penetration of impinging photons, the distribution of the first generation molecules is not homogeneous along the line defined by the excitation direction (the apparent dark peaks for 10^{-4} M, $\lambda_{exc}=294$ nm are a graphical representation artifact).

As one goes from one generation to the next, excitation further spreads and becomes closer and closer to an homogeneous distribution. Nevertheless, in all simulated cases, excitation completely decays before it becomes homogeneously distributed in space, this fact is very important to the understanding of the change in observables with both emission and excitation wavelengths.

From the spatial distribution functions obtained, definite conclusions can be drawn regarding to the effect of the concentration and of the excitation wavelength. (i) An increase of the concentration while keeping the excitation wavelength constant, leads to smaller penetration of external excitation and also to a smaller spread (owing to the decrease of the photon pathlengths). The distribution functions in the cell are thus modified (Fig. 4). (ii) If the excitation wavelength is changed while keeping the concentration constant, only the penetration of the excitation beam is affected, the pathlength of re-emitted photons remaining the same. However, all spatial distribution functions are again affected, since the distribution of the first excited molecules dictates in part the shape of those of the remaining generations. Consequently, the spatial distribution and all the observables become excitation wavelength dependent owing to radiative migration (e.g. 10^{-4} M, $\lambda_{exc}=294$ nm vs. $\lambda_{exc}=570$ nm).

B. Mean escape probabilities

Figure 5 shows the MC results for the angular dependent escape probabilities [Eq. (11)] for two 3D simulations (10^{-4} M and 10^{-3} M). The mean escape probabilities decrease in going from one generation to the next occurs mainly because each generation contains less molecules than the previous one (the fluorescence quantum yield is smaller than unity and not all emitted photons are reabsorbed). For each generation, the emission wavelength dependence of the escape probability arises from the last factor in Eq. (11), which is emission wavelength dependent: Above the absorption cutoff this factor is unitary, corresponding to no reabsorption of the emission, and under these conditions $p_n^{\Omega}(\lambda_{exc},\lambda_{em})$ reflects only the number of excited molecules of each generation. If, however, reabsorption is possible, the escape probabilities are smaller, decreasing in the increasing order of the molar absorption coefficient at λ_{em}. This is the reason why the p_n^{Ω} values always decrease when going from 650 ($\epsilon\approx20M^{-1}$ cm^{-1}) to 580 nm ($\epsilon\approx10^5$ M^{-1} cm^{-1}).

The results of Fig. 5 for 10^{-4} and 10^{-3} M solutions

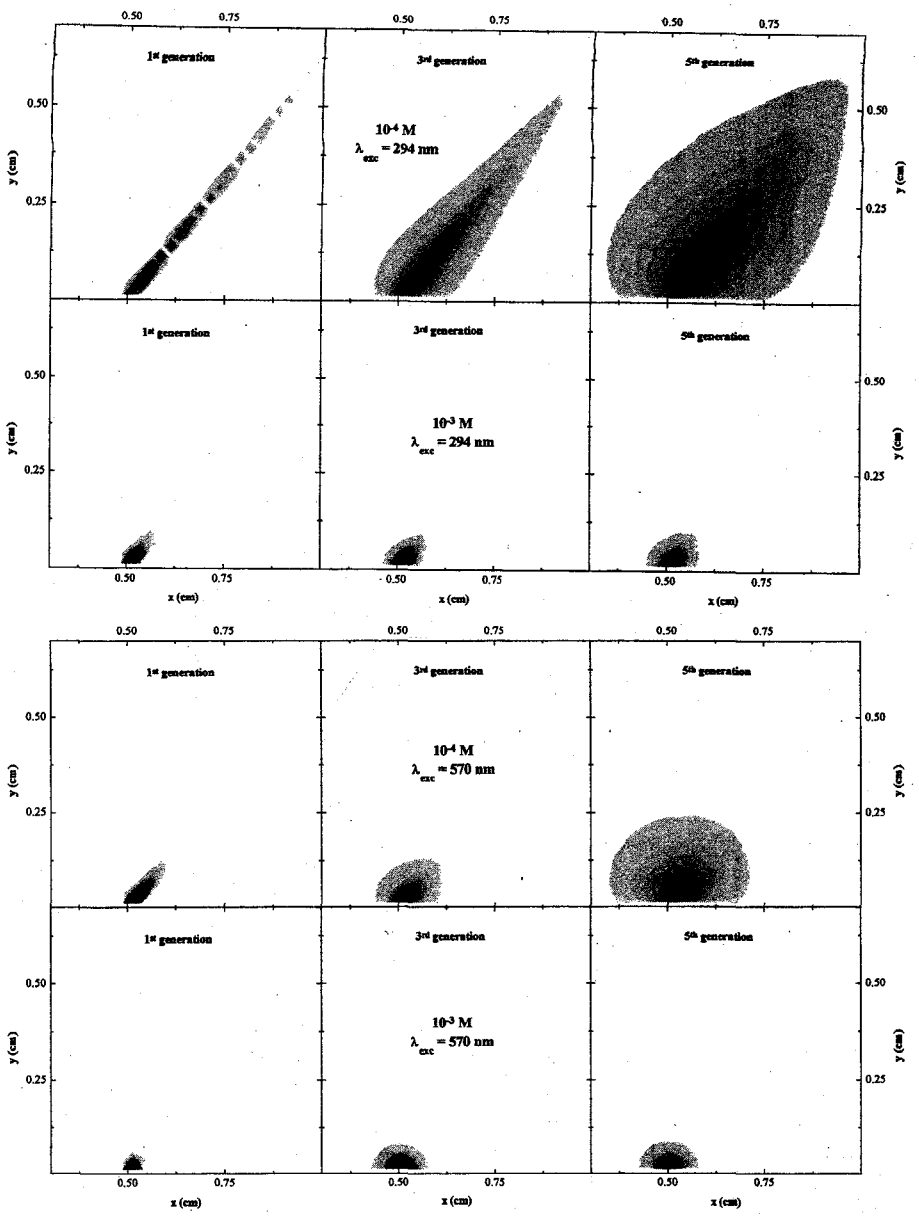

FIG. 4. Spatial distribution functions for the first, third and fifth generation of excited molecules in a front-face geometry ($\alpha' = 30°$ $\beta' = 60°$). The plots extend from 0.3 to 1 cm (x coordinate) and from 0 to 0.7 cm (y coordinate).

show also that the higher the concentration the higher the escape probabilities of photons emitted by the generations excited indirectly by reabsorption. This is a consequence of an increased importance of the radiative transport process.

The escape probabilities for the directly excited molecules are higher for the 10^{-3} M solution (notably when reabsorption is small, e.g. at 650 nm it is 0.59 for the 10^{-4} M solution and it is 0.89 for the 10^{-3} M solution). This results from the constraint of an effective cylinder for detection imposed in the 3D simulation, from the geometrical angle for fluorescence detection ($\beta' = 60°$) from the spatial distribution of excitation inside the cell. For the 10^{-3} M solution, the excitation beam is absorbed very near the wall and all of it falls inside the effective cylinder for detection. On the contrary, for the 10^{-4} M solution, the penetration is much bigger and a significant part of the external excitation is absorbed outside the region of the cell that contributes to the escape probabilities (Fig. 4).

C. Mean fluorescence lifetimes

In Fig. 6 we present the mean fluorescence lifetimes computed from the mean angular dependent escape probabilities according to Eq. (5). Note that, since we are now considering angular dependent quantities, the mean lifetime should be written as $\tau^{\Omega}(\lambda_{exc}, \lambda_{em})$. Shown in this figure are well-established results for radiative transport, namely, that the mean lifetime increases with the concentration, taking the intrinsic value only for very dilute solutions, and that it is emission wavelength dependent. The concentration depen-

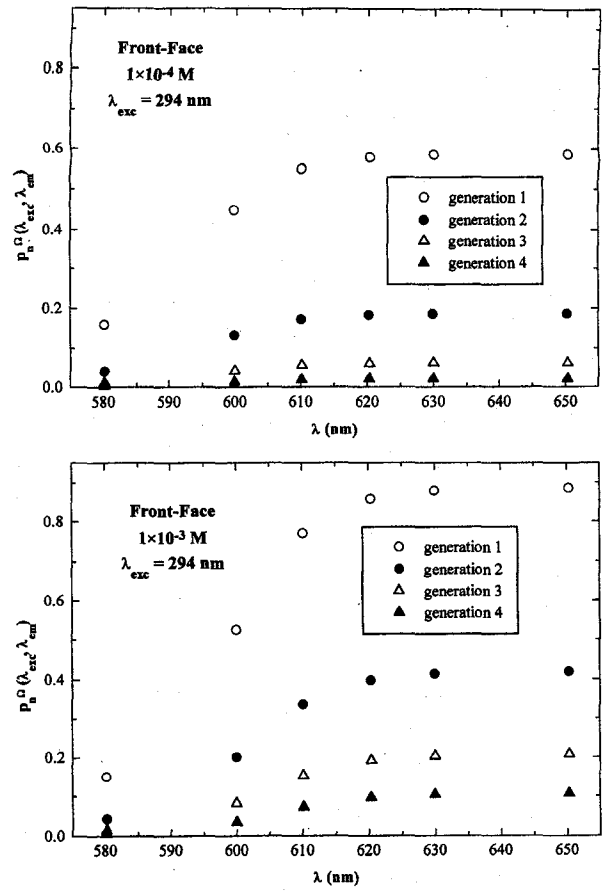

FIG. 5. Angular dependent mean escape probabilities obtained by MC 3D simulation for front-face viewing ($\alpha' = 30°$, $\beta' = 60°$) of a $1 \times 1 \times 3$ cm cell.

dence is obvious; the higher the concentration, the higher the importance of reabsorption induced imprisonment: For example, with $\lambda_{exc}=294$ nm, while for a 10^{-4} M solution only 17% of the initially excited molecules give rise to the third generation, for a 10^{-3} M solution this percentage increases to 27%. The explanation of the λ_{em} dependence comes directly from the spatial distribution of excitation. For front-face geometry, there is a progressively deeper penetration of excitation or, equivalently, the distribution of excitation moves with time into the interior of the sample cell and away from the cell wall viewed by the detection system. This does induce a selective attenuation of the radiation coming out from the cell. To discuss this effect in detail, it is necessary to consider the term is square brackets in Eq. (11). For wavelengths greater than the absorption cutoff, and since there is no reabsorption, all photon trajectories that fall inside the cylinder hit the detector. On the other hand, for wavelengths in the overlap region, the escape probabilities of the higher generations will be reduced substantially, because of the longer mean pathlength of their photons. By changing the emission wavelength we thus change the statistical weight of the different generations for the overall decay. Therefore, if reabsorption is strong, only the radiation emitted very near the wall is detected, and thus the contribution of higher generations to the observed decay is minimal, though not negligible. Table I shows the contribution of the first three generations to the steady-state intensity.

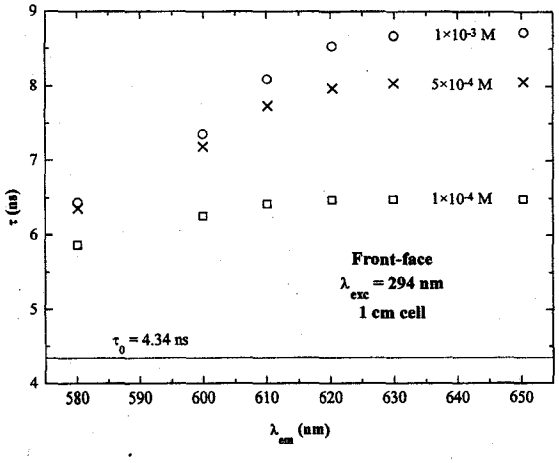

FIG. 6. Mean fluorescence lifetimes for front-face viewing ($\alpha' = 30°$, $\beta' = 60°$ as a function of concentration ($\lambda_{exc}=294$ nm).

TABLE I. Relative contribution of the first three generations to total decay. Front-face ($\alpha' = 30°$, $\beta' = 60°$) 10^{-3} M, $\lambda_{exc}=294$ nm.

Generation number	Emission wavelength			
	580 nm	600 nm	610 nm	650 nm
1	69%	60%	55%	51%
2	20%	23%	24%	24%
3	7%	9%	11%	12%

Up to now, all results presented were obtained with 3D MC simulations. As already stated, two additional geometrical possibilities were considered corresponding to a computationally more efficient unidimensional equivalent of the cell. The two unidimensional possibilities only differ in the procedure used for the computation of escape probabilities; they considered either linear pathlength or π solid angle integrated escape probabilities (see the Appendix). Table II compares the values of mean lifetimes obtained for different methods. From this table two important conclusions can be draw: the unidimensional equivalent gives always higher values for lifetimes and the two geometrical possibilities for the computation of escape probabilities in the 1D case give essentially the same result.

TABLE II. Mean fluorescence lifetimes for front-face ($\alpha' = 30°$, $\beta' = 60°$) viewing of a square ($1 \times 1 \times 3$ cm) cell computed under different geometrical approximations. $\lambda_{exc} = 294$ nm.

Concentration	λ_{em}	3D	1D + linear	1D + π angle
10^{-4} M	580 nm	5.86 ns	6.49 ns	6.35 ns
	610 nm	6.42 ns	7.98 ns	7.76 ns
	650 nm	6.49 ns	8.21 ns	8.20 ns
10^{-3} M	580 nm	6.44 ns	6.52 ns	6.38 ns
	610 nm	8.09 ns	8.58 ns	8.14 ns
	650 nm	8.72 ns	10.4 ns	10.3 ns

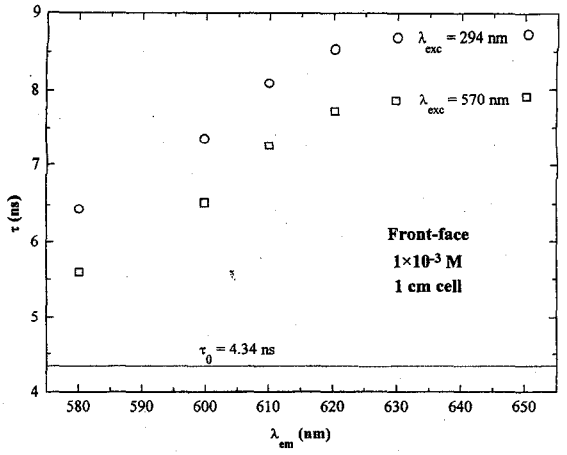

FIG. 7. Mean fluorescence lifetimes for front-face viewing ($\alpha'=30°$, $\beta'=60°$) in a MC 3D simulation of a 10^{-3} M solution at λ_{exc}=294 and 570 nm.

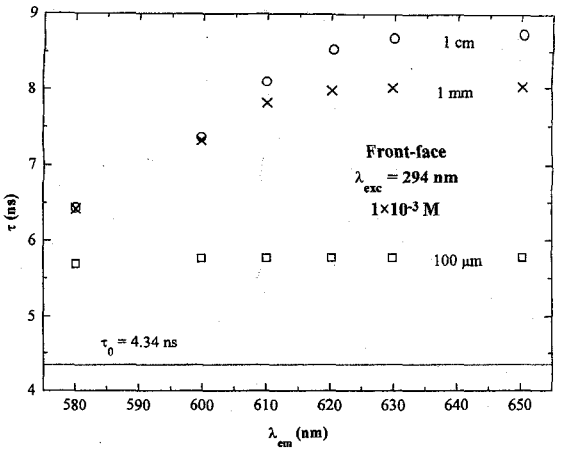

FIG. 8. Mean fluorescence lifetimes for front-face viewing ($\alpha'=30°$, $\beta'=60°$) in a MC 3D simulation of a 10^{-3} M solution excited at 294 nm. Cell thicknesses are 1 cm, 1 mm, and 100 μm.

The unidimensional simulation usually overestimates the emission lifetime. First, as already discussed, the simulation is made only in the normal coordinate to the cell wall exposed to excitation and this implies an infinite medium between two parallel limiting surfaces. We are overemphasizing radiative migration since we are neglecting escape from four of the faces of the cell. Moreover, we cannot neglect the contribution to the escape probabilities of those excited molecules that are too far from the detection apparatus for their emission to be detected. Both of these factors can be important in practice. For instance, in the conditions of Table II and for a 10^{-3} M solution (which correspond to a very small average pathlength), the 3D simulation gives rise to 27% of the external excitation reaching third generation molecules while the corresponding value for 1D simulation is 30%. In addition, the distribution of first excited molecules for a 10^{-4} M solution in Fig. 4 clearly shows that there are species whose emission can not be detected but which are considered in the unidimensional simulation anyway. Nevertheless, in the conditions of validity of the additional approximations used in the 1D equations, namely, high reabsorption (in order not to see what is happening far from the cell wall) and very low penetration (so that essentially all excitation falls inside the cell region seen by detection) the agreement is quite good all the simulations converging to a common result—for 10^{-3} M and λ_{em}=580 nm, the differences relative to the 3D case are + 1.3% (linear) and −0.8% (π integration). This shows that, at least in some conditions, the 1D simulation is a computationally more attractive way of performing the integrations.

While the emission wavelength dependence of the mean lifetimes is well known, their dependence on the excitation wavelength is not fully recognized in the literature. Figure 7 shows mean lifetimes obtained in reflection for a 10^{-3} M solution for two different values of λ_{exc}—294 and 570 nm (corresponding to a much smaller penetration of excitation since $\epsilon_{570\,nm}$ is almost ten times higher than $\epsilon_{294\,nm}$). The difference in lifetimes is roughly constant and equal to 0.83 ns, this value representing a 15% increase in the λ_{em}=580 nm lifetime when going from λ_{exc}=570 to λ_{exc}=294 nm. The λ_{exc} dependence was already considered in the discussion of Fig. 4: By changing the penetration at excitation, all the remaining factors constant, we change the distribution function of all generations (directly for first generation and indirectly for all the remaining). For instance, the change of excitation wavelength from 294 to 570 nm decreases drastically the penetration (Fig. 4); this implies that the strongly spatially asymmetric excitation is now located much more closely to the cell wall at all times, i.e., that the mean (wavelength and orientationally integrated) escape probabilities increase for all the generations decreasing by this way the global importance of reabsorption. These changes in excitation wavelength reduce the fraction of external excitation giving rise to second generation molecules from 51% to only 41%.

Figure 8 illustrates another well established fact— that the smaller the dimension the less significant is reabsorption. It shows mean lifetimes for a 10^{-3} M solution (front-face geometry) for three different cell lengths in y coordinate. Keeping dimensions constant in x and z directions, it shows results for a 1 cm, 1 mm, and 100 μm width cells. As the cell width decreases, escape probabilities increase and reabsorption becomes less important. The fraction of absorbed excitation producing second generation molecules is 51%, 45%, and 25% for 1 cm, 1 mm, and 100 μm, respectively. Figure 8 also shows that, even for a film as thin as 100 μm reabsorption cannot be neglected. Indeed, for a 10^{-3} M solution, the observed mean lifetime is 5.7 ns (at 650 nm) corresponding to a 33% increase relative to the intrinsic value (4.34 ns).

As a corollary of the discussion of the influence of experimental parameters on radiative migration, one can state the practical conditions which lead to a minimization of reabsorption: (a) thin films, (b) front-face geometry, (c) excitation wavelength at or near the absorption maximum, and (d) emission wavelength at or near the absorption maximum. The first three conditions are generally recognized, but the fourth is not, perhaps because to choose a λ_{em} where reab-

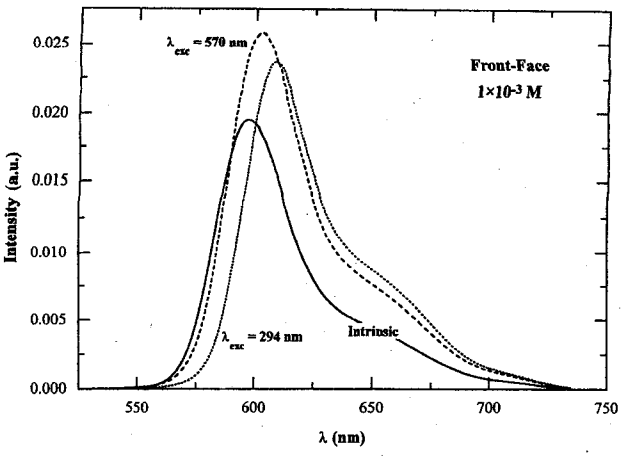

FIG. 9. Steady-state fluorescence emission spectra for front-face viewing ($\alpha'=30°$, $\beta'=60°$) in a MC 3D simulation of a 10^{-3} M solution. The emission areas are normalized to the same number of initially excited molecules.

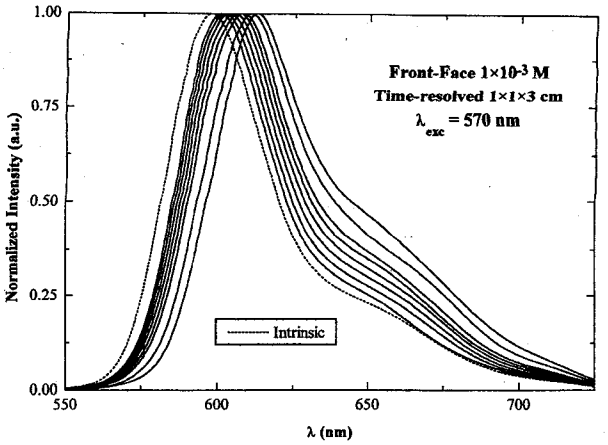

FIG. 10. Time-resolved fluorescence emission spectra for front-face viewing ($\alpha'=30°$, β' 60°) in a MC 3D simulation of a 10^{-3} M solution ($\lambda_{exc}=570$ nm). Intrinsic emission (dash) is also included for comparison. From left to right the emission times are 0, 4, 8, 12, 16, 20, 30, and 40 ns and all the spectra are normalized to maximum intensity.

sorption is maximized seems contrary to common sense. However, with such a choice the detector only receives photons coming from the very first layers of solution (near the cell wall), thus minimizing the contribution of indirectly excited molecules to the observed decay.

D. Steady-state and time-resolved fluorescence

The fluorescence intensity decay law [Eq. (4)] is in fact the δ response to excitation by an external beam of linearly polarized and essentially monochromatic light. It gives directly the time-resolved emission spectra and it can be used to obtain the response to a continuous irradiation (steady-state or photostationary-state) if the excitation beam intensity is low, that is, nonsaturating. We assume this to be valid under common practical conditions.

Figure 9 shows the simulated steady-state fluorescence spectra of a 10^{-3} M solution in a front-face viewing geometry for two different excitation wavelengths. The shape of the fluorescence spectrum changes from the intrinsic (reabsorption free) emission, $F_0(\lambda)$, the intensity being reduced in the strong reabsorption region and enhanced at longer wavelengths where reabsorption is much smaller or even nonexistent. The enhancement of fluorescence intensity at wavelengths where reabsorption is small is usually not evident from published plots due to the common practice of normalizing fluorescence spectra (normalization at the maximum or at a constant area under the spectrum being the two most common situations). Spectra in Fig. 9, on the other hand, correspond to normalized areas to the same number of initially excited molecules, the differences to intrinsic emission being solely the result of reabsorption–re-emission processes, that direct more photons towards the detector.

Figure 9 clearly shows that, for concentrated media, steady-state emission is also excitation wavelength dependent—for higher penetration of external excitation (294 nm) the average pathlength of the detected radiation is higher and, as a consequence, the attenuation in the strong reabsorption region is more important. This shows the importance of stating the excitation wavelength when reporting fluorescence spectra of concentrated solutions, an often neglected point.

Figure 10 shows time-resolved simulated spectra for a 10^{-3} M solution together with the reabsorption free emission (all data normalized at the maximum intensity). In the blue region of the spectrum (where reabsorption is possible) the fluorescence intensity is lower for longer times which reflects the time evolution of the spatial distribution functions. As time progresses, molecules become gradually deeper located, hence the average pathlength of the outcoming photons is also gradually growing with time increasing their reabsorption probability within the reabsorption region. In this figure, the 0 ns time spectrum is already reabsorption distorted from the molecular emission. This happens because we are neglecting the finite time for light propagation in cell (of course, the *exactly* zero time spectrum should be equal to molecular emission since zero time emission could only result from molecules standing at the cell wall). Nevertheless, since one is working in a ns time scale and since the lengths involved are quite small, the neglect of the light propagation time is a valid assumption.

E. Macroscopic quantum yield

Angular and emission wavelength integrated escape probabilities allow the computation of the macroscopic, orientationally averaged fluorescence quantum yield [Eq. (9)]. Since it is common practice to use integrated steady-state emission areas to estimate quantum yields by relative methods, we have chosen also to compute some technical parameters being given by the area under the photostationary emission normalized to a Φ_0 molecular fluorescence area and to the same number of initially excited molecules ($\Phi_{technical}$). These values are given in Table III.

The macroscopic, orientationally averaged quantum yield (Φ_{real}) is unambiguously defined as the ratio of the

TABLE III. Macroscopic, orientationally averaged (real) and technical quantum yields for front-face (α' 30°, $\beta'=60°$) viewing of a square (1 $\times 1 \times 3$ cm) cell as a function of concentration, λ_{exc} and y dimension.

Concentration	λ_{exc}	Thickness	Φ_{real}	$\Phi_{technical}$
10^{-4} M			81%	73%
5×10^{-4} M	294 nm	1 cm	77%	107%
10^{-3} M			76%	113%
10^{-4} M			83%	108%
5×10^{-4} M	570 nm	1 cm	80%	120%
10^{-3} M			79%	124%
		1 cm	76%	113%
10^{-3} M	294 nm	1 mm	79%	107%
		100 μm	85%	99%

number of emitted photons that come out from the cell to the number of excitation photons absorbed. The presence of radiative transport in concentrated media renders this value different from the molecular quantum yield and also dependent on the geometry of the cell. Quantum yield is no longer a property essentially characteristic of the chromophore but becomes dependent on factors such as shape and dimension of the cell, wavelength, and excitation geometry.

This quantum yield is of necessity lower than the molecular one since for each reabsorption–re-emission there is a probability $1-\Phi_0$ of non-radiative decay. So, the more important the radiative migration, the lower Φ_{real}. This can be seen in Table III since (a) increasing concentration, (b) increasing penetration, or (c) increasing dimension of the cell reduces Φ_{real}.

On the other hand, the possibility of reabsorption allied with the occurrence of highly inhomogeneous spatial distribution of excited species (in all cases excitation effectively dies before an homogeneous distribution is reached) makes the overall steady-state fluorescence intensity very sensitive on the collecting geometry. Indeed, owing to reabsorption, the fluorescence of the initially excited molecules is only partially detected but, because of re-emission events, the number of initial photons lost can be counterbalanced or even surpassed (over the particular collecting solid angle considered) by the number of subsequently detected re-emitted photons. One conclusion can be draw from Table III: whenever the excitation is highly concentrated near the cell's face probed by detection, the detected fluorescence intensity overestimates the overall angular integrated intensity, this effect leading to apparent emission yields which can be significantly higher than 1. This fact effectively hinders the use of relative methods relying on the comparison of emission areas to estimate quantum yields unless one makes a 4π spatial integration of the detected fluorescence.

F. Time-resolved and steady-state anisotropies

Figure 11 shows time-resolved fluorescence emission anisotropies [Eq. (14)] and Fig. 12 mean anisotropy decay

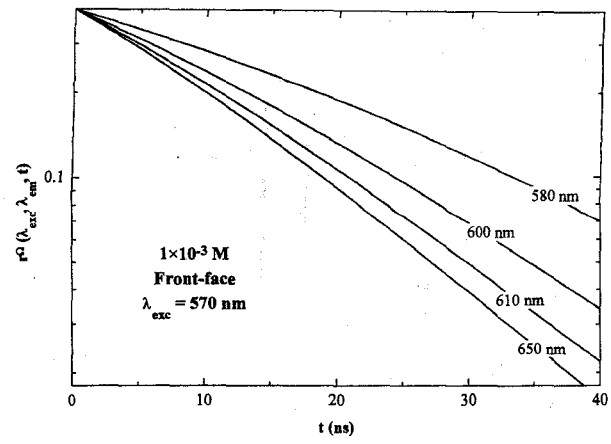

FIG. 11. Time-resolved fluorescence anisotropy decay for front-face viewing ($\alpha'=30°$, $\beta'=60°$) in a MC 3D simulation of a 10^{-3} M solution ($\lambda_{exc}=570$ nm).

times, defined analogously to the mean lifetimes of fluorescence [Eq. (5)], but using the anisotropy decay Eq. (14) instead of the fluorescence intensity decay.

Figure 11 clearly shows an emission wavelength dependent anisotropy decay, the difference in wavelength behavior coming from the fact that the relative statistical weight of the higher generations to the observed decay is λ_{em} dependent. The lower the reabsorption at λ_{em}, the more important the indirectly excited molecules (carrying out a lower anisotropy since in each emission–reabsorption event there is a 100%−28%=72% reduction of fluorescence anisotropy) leading to a faster anisotropy decay.

Figure 12 quantifies the effect of radiative migration on fluorescence anisotropy data. The faster the anisotropy decay (higher concentration and/or lower reabsorption), the shorter the decay time (in the absence of reabsorption, the anisotropy decay time is infinite).

Finally, Fig. 13 shows the predicted values for the steady-state fluorescence anisotropy indicating again that the higher the contribution of radiative migration to observables,

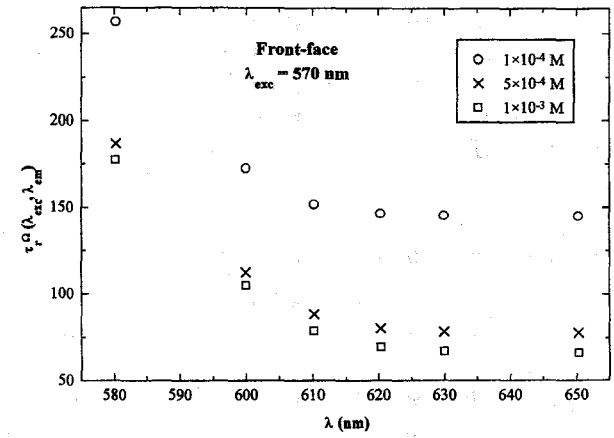

FIG. 12. Mean anisotropy decay lifetimes for front-face viewing ($\alpha'=30°$, $\beta'=60°$) in a MC 3D simulation as a function of concentration (λ_{exc} = 570 nm).

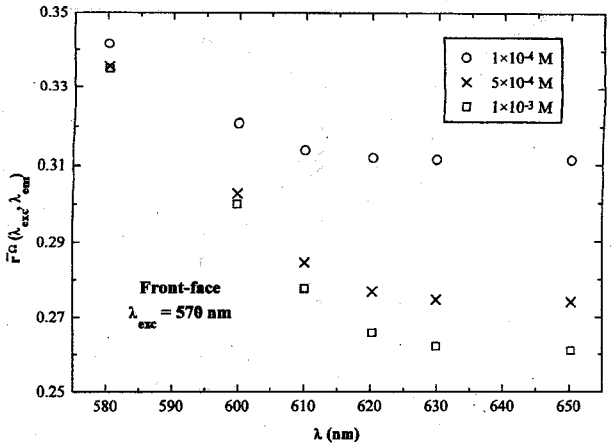

FIG. 13. Steady-state anisotropy values for front-face viewing ($\alpha'=30°$, $\beta'=60°$) in a MC 3D simulation a function of concentration ($\lambda_{exc}=570$ nm).

the lower the steady-state anisotropy. Interestingly, the steady-state anisotropy is high even for the 10^{-3} M solution (ranging from 0.26 to 0.33). This occurs because the polarization retained after one transfer step is significant (28%), seven times greater than that retained after one transfer by the nonradiative dipole–dipole transfer mechanism.

All the anisotropy results presented refer to an excitation wavelength of 570 nm. This ensures that the fluorescence anisotropy of directly excited molecules (fundamental anisotropy) corresponds to the theoretical value of 0.4 since the absorption and emission transition dipole vectors are parallel.

V. RIGHT-ANGLE GEOMETRY

A. Spatial distribution functions

Figure 14 shows contour plots of the spatial distribution functions of selected generations. The picture of the excitation spread as one goes from one generation to the next is entirely analogous to the one described in the discussion of Fig. 4, the main difference resulting from the fact that now external excitation is normal to cell wall. As for front-face geometry, the distribution functions are excitation wavelength dependent as one can see by comparison of the first and last rows of Fig. 14.

B. Mean escape probabilities

The simulated angular dependent escape probabilities [Eq. (11)] are shown in Fig. 15. The explanation for the dependence of $p_n^{\Omega}(\lambda_{exc},\lambda_{em})$ on λ_{em} and generation number is the same as the one found for front-face, the main difference being the fact that escape for λ_{em} values where reabsorption is strong is much smaller due to the much bigger path length in cell prior to escape (this path length for the directly excited molecules is exactly 0.5 cm).

C. Fluorescence decays and mean fluorescence lifetimes

The fluorescence intensity decays for the right-angle geometry present interesting features. Some simulated decays (normalized at maximum intensity) are shown in Fig. 16 for a 10^{-4} M solution, as a function of the emission wavelength. This figure clearly shows the importance of this parameter on the emission decay. The decays at wavelengths where rhodamine 101 absorption is strong contain an initial rise time component not observed for longer wavelengths where reabsorption is smaller. This rise time, never observed in front-face geometry, arises from the interplay between the spatial distribution of excitation and the detection geometry:

The emission from directly excited molecules must travel a distance of 0.5 cm before being detected. When the optical density at λ_{em} is high enough, practically all the photons are reabsorbed before reaching the detector. This means in practice that the first generation does not contribute at all to the observed decay. But because of the spread of excitation (Fig. 14), the subsequent generations are much closer to the cell wall, and contribute to the intensity decay.

In contrast, for front-face, since excitation is walking away from the cell wall under detection, the average path length for reabsorption is always increasing with generation number. This means that, no matter what emission wavelengths we consider, first generation molecules always contribute more to the observed decay than the higher number generations. So, as a consequence, for reflection geometry there can be no rise time.

Figure 17 shows the predicted mean fluorescence lifetimes obtained for a 3D integration computed from the corresponding escape probabilities and from Eq. (5). In this figure, escape probabilities were always computed for a 5 mm diameter cylinder centered at (and normal to) the cell wall facing the detector. At sufficiently dilute solutions (10^{-5} M) no rise time is observed; at intermediate cases (5×10^{-5} and 10^{-4} M, where optical density in the strong reabsorption region can be high enough to preclude escape of the first generation radiation but, however, is not sufficiently high at λ_{exc} to preclude external excitation to reach the middle of the cell—Fig. 14) decays can have a rise-time in the blue part of the spectrum and, finally, if the concentration is so high (5×10^{-4} M) that the external excitation cannot reach the middle of the cell (Fig. 14), then, irrespective of the emission wavelength, an initial risetime is always observed.

As a corollary of this discussion, Figs. 14 and 17 clearly show that the λ_{exc} dependence of the decay is critical in this geometry. For instance, for a concentration as low as 5×10^{-5} M and if the optical density at λ_{exc} is high enough to induce complete absorption near the cell wall (last row of Fig. 14 with $\lambda_{exc}=570$ nm) then a risetime is expected even for λ_{em} corresponding to no reabsorption.

Although the existence of risetimes has never been unambiguously identified with radiative transport in the literature, some experimental results nevertheless do exist. Reabsorption is probably the explanation for the risetime

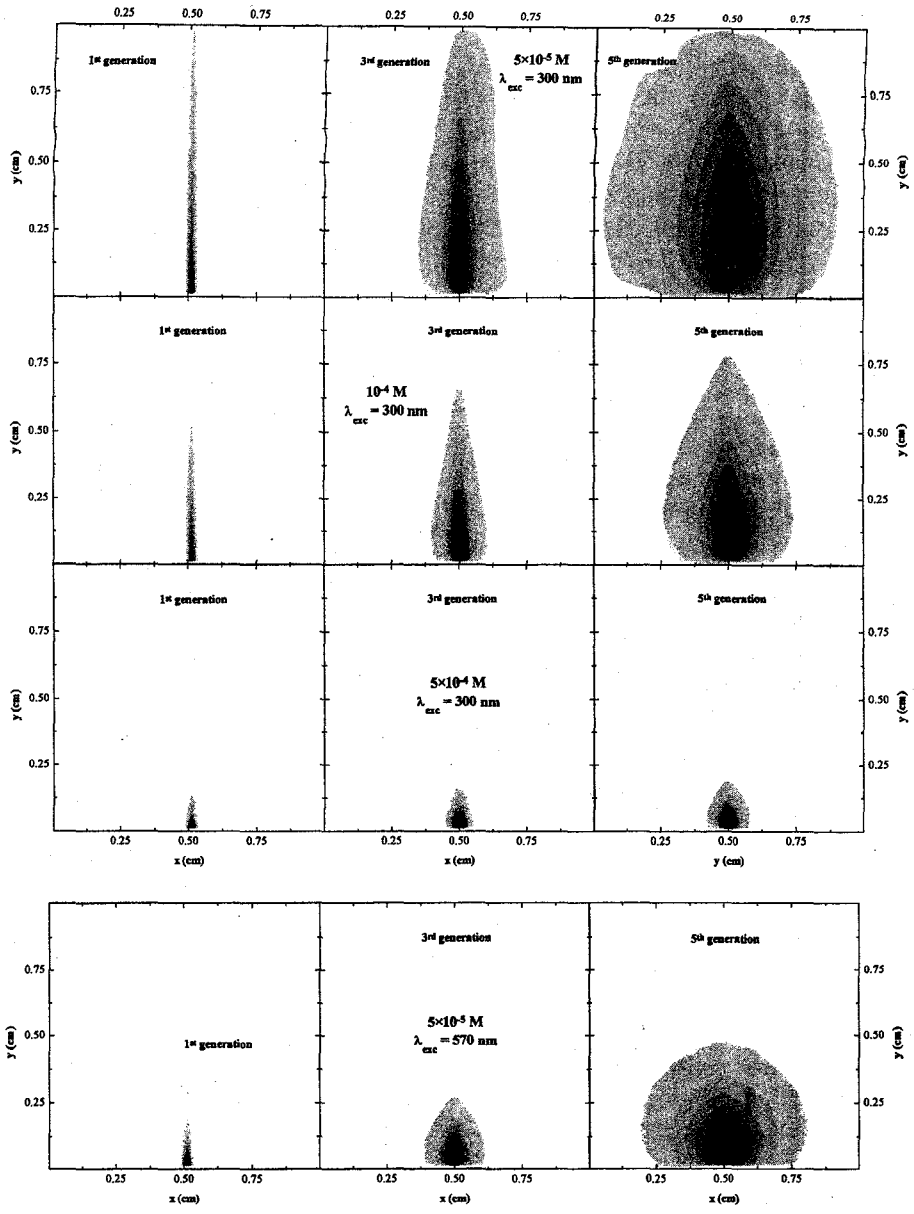

FIG. 14. Spatial distribution functions for the first, third and fifth generation of excited molecules in a right-angle geometry. The plots extend over the full dimensions of the experimental cell.

observed in some fluorescence decays of rhodamine B[7] and rhodamine 575.[8]

The experimental observation of risetimes is hampered by the low fluorescence intensities in the overlap region, as Fig. 14 shows. However, experimental results for this region showing clear rise times, were recently obtained in our laboratory for the system under study.[9]

D. Time-resolved and steady-state anisotropies

Fluorescence anisotropy in the presence of radiative migration becomes emission wavelength dependent, as mentioned. Figure 18 shows time-resolved emission anisotropies computed from Eq. (14) and Fig. 19 mean anisotropy decay times.

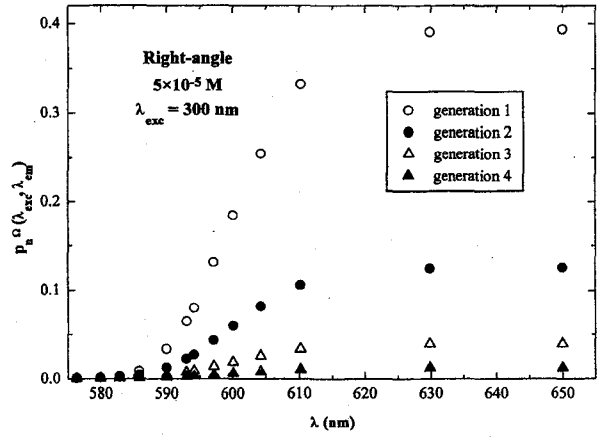

FIG. 15. Angular dependent mean escape probabilities for right-angle viewing of a 1×1×3 cm cell. Escape probabilities obtained by MC 3D integration.

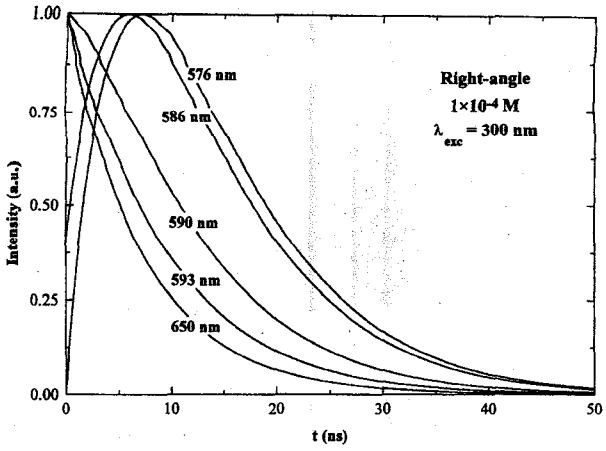

FIG. 16. Simulated fluorescence intensity decays for right-angle geometry of a 10^{-4} M solution as a function of the emission wavelength.

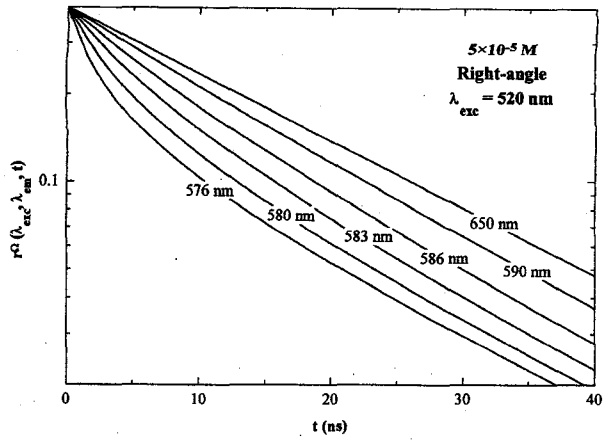

FIG. 18. Time-resolved fluorescence anisotropy decay for right-angle geometry in a MC 3D simulation of a 5×10^{-5} M solution (λ_{exc}=520 nm).

As already discussed for the case of front-face viewing, the relative importance of each individual generation to the overall decay data is a function of λ_{em} and this manifests itself in anisotropy decays. The higher the contribution of indirectly excited molecules the faster the anisotropy decay. This leads to a reversal of the order found for the λ_{em} dependence, relative to front face: in right angle the fastest anisotropy decays correspond to strong reabsorption (Figs. 18 and 19) while for front face strong reabsorption is connected with the slowest decays (Figs. 11 and 12). Again, the explanation comes from spatial distribution functions. In front face, the excitation is going away from the cell wall viewed by detection. This means that for high reabsorption, what happens deep inside the cell is not seen by the detector, thus effectively minimizing the contribution of high order generations. For right-angle geometry, excitation walks towards the cell wall facing the detector. In such conditions, weak reabsorption minimizes the contribution of indirectly excited molecules and leads to a slower anisotropy decay.

The λ_{em} dependence is also evident in the predicted values of the steady-state anisotropy, the same reasoning applying to the results shows in Fig. 20. The range of values spanned by the steady-state anisotropy of a particular solution (notably 5×10^{-5} and 10^{-4} M in Fig. 20) is higher for right angle than for front face angle (compare Figs. 13 and 20). This comes from the fact that, on the average, the right angle detected radiation can suffer reabsorption over a much longer path length.

VI. SUMMARY AND CONCLUSIONS

The available theoretical treatment of radiative transport allows in principle the accurate prediction of the fluorescence intensity and anisotropy decays, and of the fluorescence spectrum and macroscopic quantum yield, under given conditions, and provided the enunciated assumptions are obeyed. However, most of the coefficients of the theoretical expressions are in general not amenable to analytic form, and even their numeric computation is quite difficult. Given the probabilistic nature of the underlying processes of absorption and emission, a Monte-Carlo simulation built upon the basic theoretical equations is particularly well suited for the task. Because of the factorization of space and time dependencies

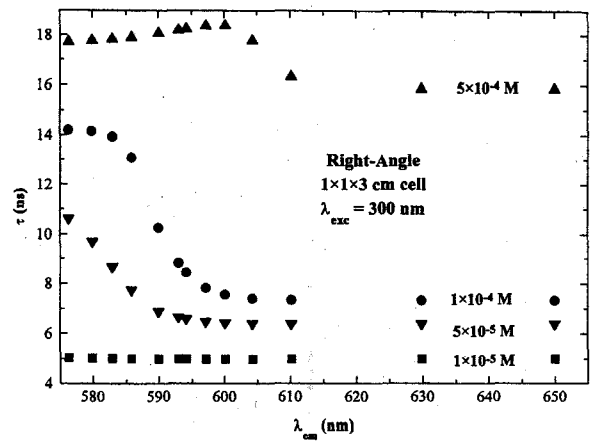

FIG. 17. Mean fluorescence lifetimes for right-angle viewing as a function of concentration (λ_{exc} kept constant at 300 nm).

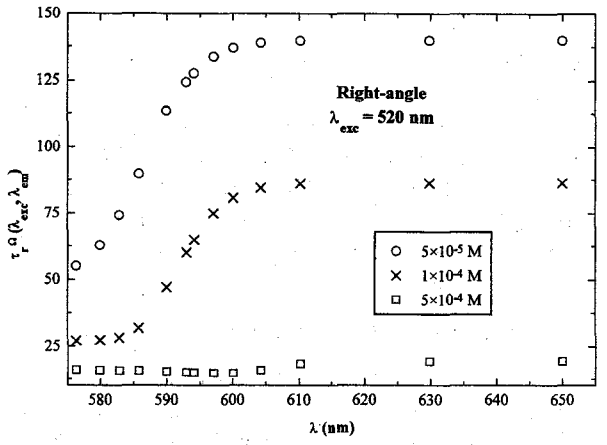

FIG. 19. Mean anisotropy decay lifetimes for right-angle geometry in a MC 3D simulation as a function of concentration (λ_{exc} = 520 nm).

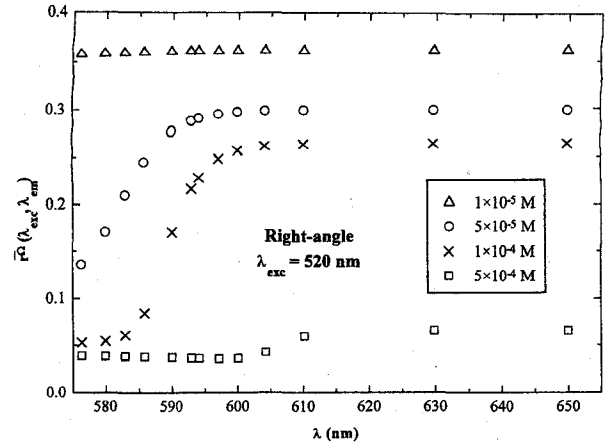

FIG. 20. Steady-state anisotropy values for right-angle geometry in a MC 3D simulation as a function of concentration (λ_{exc}=520 nm).

in the central quantity $\rho_n(\lambda_{exc},\lambda_{em},t)$ [Eq. (2)] and since the exact time dependence is known [Eq.(3)], the simulation procedure can be restricted to the spatial aspects of radiative transport, resulting in an important gain in simulation efficiency. In this work, we discussed and carried out detailed simulations for a realistic system (rhodamine 101 in ethanol) in a finite three-dimensional volume that reproduces a common fluorescence cell. The two usual geometries of detection were considered: front face and right angle. The system chosen is particularly interesting because it combines several factors favoring radiative transport—high absorption-emission spectral overlap (ca. 87%), high fluorescence quantum yield (89%) and high molar absorption coefficients in the overlap region.

The MC simulation method developed allowed, for the first time, the accurate calculation of the effect of radiative transport on fluorescence intensity and anisotropy decays, time-resolved and steady-state spectra, as well as on the values of the macroscopic quantum yield and steady-state anisotropy. Because the spatial distribution of each generation of excited molecules could also be obtained with this method, a direct and clear picture of the spatial evolution of the excitation was also obtained.

Because part of the factors that favor radiative transport (high absorption–emission spectral overlap, high fluorescence quantum yield and high molar absorption coefficients in the overlap region) tend to yield a significant Förster radius for self-transfer, nonradiative transport by the dipolar mechanism may also be present. This process of transport is significant whenever the average distance between molecules is of the order or smaller than the Förster radius for self-transfer. It is therefore important to assess its effect on the global response of the system. In a system where both mechanisms are operative, the excitation will perform series of short hops by the nonradiative mechanism, alternated with long distance jumps by the radiative one. A unified treatment of the kinetics of this problem is wanting, but some approximate results can be easily obtained. Regarding the decay law, the existence of nonradiative hops has no effect on it. In fact, it is well known that a pure nonradiative transport process *leaves the decay law unchanged.*[10] *Furthermore, the hops are* performed locally (the excitation spread being usually of a few average molecular distances) and thus the excitation does not move significantly in macroscopic terms. Another consequence of the nonradiative hops is the efficient randomization of the orientation of the emitting dipole. In this way, and depending on the importance of the nonradiative transport mechanism, the assumption of isotropic emission may be appropriate even in rigid media.[11,12] All these results show that the fluorescence decay model developed here for pure radiative transport still applies in the presence of nonradiative transport. As regards the anisotropy decay, the contribution of nonradiative transport may on the contrary be non-negligible, as stated previously (Sec. II D). The results presented for rhodamine 101 in ethanol considered only the contribution of radiative transport on the anisotropy. In fact, for some of the concentrations used, there is also a significant depolarization from nonradiative transport: Using the computed Förster radius for self-transfer (58 Å), the steady-state anisotropies are predicted to be[13] 95% (10^{-4} M), 76% (5×10^{-4} M), and 64% (10^{-3} M) of the maximum value (0.4), only on account of nonradiative transport. Clearly, the experimental anisotropy of the simulated system will be smaller than any of the values separately computed for radiative and nonradiative transport, but a theoretical treatment of the combined effect of radiative and nonradiative transport on the fluorescence anisotropy is not presently available. Work in this direction is in progress.

ACKNOWLEDGMENTS

This work was supported by JNICT (Junta Nacional de Investigação Científica e Tecnológica, Portugal) and FEDER (Fundo Europeu para o Desenvolvimento Regional, União Europeia) through research Contract No. STRDA/C/CEN/421/92 and (EJNP) JNICT BD/2242/92-RM.

APPENDIX: UNIDIMENSIONAL SIMULATION

The MC procedure is the same for both the 3D and its unidimensional equivalent simulation programs. The 1D simulation differs only in (a) the equation describing the absorption coordinates of external excitation, (b) the step transition probability, and (c) the escape probabilities.

The external excitation absorption coordinate is given by Eq. (17). The step transition probability was already derived in Paper I of this work.[1] Consider Fig. 1: The absorption probability at y_i of a photon emitted at y_{i-1} is obtained by integration of Eq. (7) over the xz plane containing y_i

$$f(y_i|y_{i-1},\lambda_{i-1}) = \tfrac{1}{2}\varepsilon(\lambda_{i-1})C\ln 10 \times \int_1^\infty \frac{10^{-\varepsilon(\lambda_{i-1})C|y_i-y_{i-1}|u}}{u}du \quad \text{(A1)}$$

which can be thought of as a modified version of the Beer–Lambert law.

The implementation of the transformation method over Eq. (A1) to compute reabsorption coordinates was made as

follows. First, an uniform deviate r was used to decide the emission direction, left ($r<1/2$) or right (otherwise). The integrated distribution obtained from Eq. (A1) is (neglecting the 1/2 term):

$$F(\Delta y,\lambda_{i-1})=(1-10^{-\varepsilon(\lambda_{i-1})C\Delta y})+\varepsilon(\lambda_{i-1})C\ \ln 10\ \Delta y \times\int_1^{\infty}\frac{10^{-\varepsilon(\lambda_{i-1})C\Delta yu}}{u}du, \tag{A2}$$

where $\Delta y=|y_i-y_{i-1}|$ and the integral term in Eq. (A2) is related with the exponential integral function. In this equation the first term is simply the integrated distribution corresponding to the usual 1D Beer law, the last term representing an additional correction.

Since the exponential integral can only be evaluated numerically, $F(\Delta y,\lambda_{i-1})$ has no analytical inverse function and the photon path length must be given numerically in a similar way of that used for the wavelength of reemitted fluorescence.

In the unidimensional simulation two cases were considered for the estimation of escape probabilities. First, the usual Beer–Lambert law was considered along a linear path length defined according to the emission coordinates and with Snell's refraction at the cell boundary—escape probability given by Eq. (18). An additional possibility was considered corresponding not to escape along a single line but rather along a π solid angle (escape from the left cell wall in Fig. 2). For this case, the escape probability is given by[4(a)]

$$p_{esc}(y,\lambda_{em})=\frac{1}{2}\int_1^{\infty}\frac{10^{-\varepsilon(\lambda_{em})Cyu}}{u^2}du \tag{A3}$$

as a function of the emission coordinate (y) inside the 1D cell.

[1] M. N. Berberan-Santos, E. J. Nunes Pereira, and J. M. G. Martinho, J. Chem. Phys. **103**, 3022 (1995).
[2] F. James, Rep. Prog. Phys. **43**, 1145 (1980).
[3] W. H. Press, S. A. Teukolsky, W. T. Vetterling, and B. P. Flannery, Numerical Recipes, 2nd ed. (Cambridge University, Cambridge, 1992).
[4] (a) E. J. Nunes Pereira, M. N. Berberan-Santos, and J. M. G. Martinho, J. Lumin. **63**, 259 (1995); (b) M. N. Berberan-Santos and M. J. E. Prieto, J. Chem. Phys. **88**, 6341 (1988).
[5] T. Holstein, Phys. Rev. **72**, 1212 (1947).
[6] P. Lévy, *Théorie de l'addition des Variables Aléatoires* (Gauthier-Villars, Paris, 1954).
[7] Y. Sakai, M. Kawahigashi, T. Minami, T. Inoue, and S. Hirayama, J. Lumin. **42**, 317 (1989).
[8] (a) J. S. Batchelder, A. H. Zewail, and T. Cole, Appl. Opt. **18**, 3090 (1979); (b) J. S. Batchelder, A. H. Zewail, and T. Cole, *ibid.* **20**, 3733 (1980).
[9] E. J. Nunes Pereira, M. N. Berberan-Santos, and J. M. G. Martinho (unpublished).
[10] Th. Förster, Ann. Phys. **2**, 55 (1948).
[11] The rotational correlation time of rhodamine 101 in ethanol at room temperature is ca. 170 ps, while the intrinsic lifetime is 4.3 ns. The assumption of isotropic emission for the conditions of simulation is therefore justified even in the complete absence of non-radiative transport.
[12] Note, however, that in rigid media, especially glasses, inhomogeneous broadening, not considered in the model, may be significant, see, for example, A. D. Stein, K. A. Peterson, and M. D. Fayer, Chem. Phys. Lett. **161**, 16 (1989), M. N. Berberan-Santos, J. Canceill, E. Gratton, L. Jullien, J. M. Lehn, P. So, J. Sutin, and B. Valeur, J. Phys. Chem. **100**, 15 (1996), and references therein.
[13] G. H. Fredrickson and C. W. Frank, Macromolecules **16**, 1198 (1983).